Limited underthrusting of India below Tibet: ^{3}He/^{4}He analysis of thermal springs locates the mantle suture in continental collision

Simon L. Klemperer[a,1], Ping Zhao (赵平)[b,1], Colin J. Whyte[c], Thomas H. Darrah[c], Laura J. Crossey[d], Karl E. Karlstrom[d], Tianze Liu (刘天泽)[a,e], Carmen Winn[d,2], David R. Hilton[e,3], and Lin Ding (丁林)[b]

During continent–continent collision, does the downgoing continental plate underplate far inboard of the collisional boundary or does it subduct steeply into the mantle, and how is this geometry manifested in the mantle flow field? We test conflicting models for these questions for Earth's archetypal continental collision forming the Himalaya and Tibetan Plateau. Air-corrected helium isotope data (^{3}He/^{4}He) from 225 geothermal springs (196 from our group, 29 from the literature) delineate a boundary separating a Himalayan domain of only crustal helium from a Tibetan domain with significant mantle helium. This 1,000-km-long boundary is located close to the Yarlung-Zangbo Suture (YZS) in southern Tibet from 80 to 92°E and is interpreted to overlie the "mantle suture" where cold underplated Indian lithosphere is juxtaposed at >80 km depth against a sub-Tibetan incipiently molten asthenospheric mantle wedge. In southeastern Tibet, the mantle suture lies 100 km south of the YZS, implying delamination of the mantle lithosphere from the Indian crust. This helium-isotopic boundary helps resolve multiple, mutually conflicting seismological interpretations. Our synthesis of the combined data locates the northern limit of Indian underplating beneath Tibet, where the Indian plate bends to steeper dips or breaks off beneath a (likely thin) asthenospheric wedge below Tibetan crust, thereby defining limited underthrusting for the Tibetan continental collision.

continental collision | Tibetan plateau | mantle helium | structural seismology | Indian lithosphere

One long-standing seismologically driven model of the Himalaya–Tibet orogen—and by implication other continental collisions—is that the Indian plate underplates (underthrusts) much or all of the Tibetan Plateau, implying the lithospheric mantle below Tibet is cratonic Indian mantle (1, 2) (Fig. 1A). In an alternative model and description of mountain building, also seismologically driven, India plunges steeply into the mantle (subducts) beneath southernmost Tibet, implying the mantle beneath most of Tibet is "orogenic" and hot (3, 4) (Fig. 1B). An essential difference is whether there is an asthenospheric mantle wedge between the Tibetan crust and the downgoing Indian plate (Fig. 1B). Here we show with helium isotope data that India subducts beneath an asthenospheric wedge that underlies three-quarters of the Tibetan Plateau.

In Tibet, numerous seismological studies offer conflicting locations of the "mantle suture" [southern limit of orogenic or asthenospheric mantle at the Moho (5)] and hence the extent of incorporation of Indian continental lithosphere into the Tibetan Plateau (1–7) (Fig. 1 A and B). Seismic wavespeed in the mantle is largely a proxy for temperature (8), and some interpret a south-to-north P-wavespeed decrease beneath southern Tibet as marking the northern leading edge of Indian subduction and the mantle suture (3) (red line, Fig. 1C), whereas others focus on the continuity from northern India to northern Tibet of surface-wave velocities down to >200-km depth that are consistent with a lithospheric mantle lid (2) (blue line, Fig. 1C).

Here we use helium-isotope ratios (^{3}He/^{4}He) measured in all accessible warm and hot springs in Tibet collected across diverse geologic settings such as suture zones, rifts, different host rocks, and different proximity to crustal intrusions. Our data explore the deep structure of the Himalaya and Tibet crucial to understanding the development of the world's largest mountain belt. Our hypothesis is that a "mantle suture" between cold Indian mantle and a hot orogenic Tibetan mantle wedge (Fig. 1B) should be identifiable by a boundary or transition at Earth's surface between groundwaters containing entirely crustal ^{3}He/^{4}He ratios and a domain with resolvable primordial mantle ^{3}He that has ascended from the mantle wedge. We build on similar studies in the Andes that also used helium isotopes from hot springs above a subducting plate to delineate a boundary between crustal-derived and mantle-derived helium domains (9). An

Significance

Our regional-scale geochemical dataset (^{3}He/^{4}He) resolves the geometry of the continental collision between India and Asia. Geophysical images have led to contradictory interpretations that India directly underthrusts Tibet as a horizontal plate or India subducts steeply into the mantle. Helium transits from mantle depths to the surface within a few millennia, such that the ratio of mantle-derived ^{3}He to dominantly crust-derived ^{4}He provides a snapshot of the subsurface. ^{3}He/^{4}He data from 225 geothermal springs across a >1,000-km-wide region of southern Tibet define a sharp boundary subparallel to the surface suture between India and Asia, just north of the Himalaya, delineating the northern limit of India at ~80-km depth. The India–Asia collision resembles oceanic subduction with an asthenospheric mantle wedge.

Fig. 1. Alternative geometries of continental collision, and location map. (*A* and *B*) Cartoons defining "underthrusting," "subduction," and "mantle suture" [boundary of Indian lithosphere with (*A*) Tibetan lithosphere or (*B*) asthenosphere]. Blue: cratonic lithosphere (cold); red: asthenosphere (hot). (*C*) Map (same area as Fig. 3) locating cross-section in Fig. 4 (yellow swath) and previous seismic interpretations: red: mantle suture from body-wave tomography (3); green: crustal front from receiver-functions (7); blue: northern limit of 240-km-thick Indian lithosphere produced by pure-shear shortening (2) intended to reproduce lithospheric thickness mapped by Rayleigh-wave tomography (8). Thin gray lines: sutures/major faults, south to north. MFT, Main Frontal Thrust; STD, South Tibet Detachment; YZS, Yarlung-Zangbo Suture; BNS, Banggong-Nujiang Suture; JRS Jinsha River Suture and major strike-slip faults ATF (Altyn Tagh), KF (Kunlun), and KKF (Karakoram). Thick gray lines: active rifts: YR, Yare; TG, Thakkola graben; LG, Lunggar graben; TY, Tangra-Yumco; PX, Pumco-Xainza; YG, Yadong-Gulu; CS, Cona-Sangri. Colored circles and triangles correspond to geologic terranes and match symbols in Fig. 2 and *SI Appendix*, Figs. S2 and S5.

equivalent surface boundary has also been found in Japan, above the subducting Pacific and Philippine Sea plates (10), that bounds a region of high mantle ^{3}He correlated with low seismic wavespeeds in the mantle (10). We build on earlier helium-isotope mapping in Tibet (11, 12) but with an order-of-magnitude more data across more diverse geologic settings to allow a continuous and more precise delineation of isotopic boundaries. Our broad geographic coverage spanning 1,500 km demonstrates that different helium domains are not associated with local geology or crustal terrane boundaries, thereby showing that measured ^{3}He does not represent the modern release of ^{3}He preserved within the crust from an earlier geologic period. Our database includes 86 springs from which samples air-corrected using ^{20}Ne unequivocally show the presence of mantle-derived helium (*SI Appendix*, Table S1).

The result is a geochemically constrained sharp boundary between a Himalayan domain of only crustal helium to the south and a Tibetan domain with mantle helium to the north. This boundary parallels the geologically defined suture zone for over 1,000 km across Tibet and resolves competing geophysical interpretations for the location of the mantle suture. Our boundary agrees best with tomographic images utilizing body waves (3, 6) and coincides with and helps explain both the northern limit of >65-km-deep earthquakes in the Indian plate (13) and the change in seismicity from dominantly normal faulting in southern Tibet to dominantly strike-slip faulting in central Tibet (14).

Results

New ^{3}He/^{4}He Data in Tibet. Tibet forms one of Earth's great geothermal provinces, with over 700 warm, hot, and boiling springs (15). In Tibet, local topography drives advective flow to depths of 2 to 5 km (16, 17) so that even the hottest springs require no heat source beyond topographically driven penetration into a crust of average continental heat flux 60 to 90 mW·m^{-2} (17). Thus, spring temperatures largely represent depth of groundwater circulation and the extent of mixing between meteoric (shallow) and deeply sourced groundwaters. We systematically sampled 196 distinct spring systems (*Materials and Methods*), some not previously known to science, at elevations up to 5,630 m and temperatures of 6 to 93 °C spanning

1,500 km along- and 500 km across-strike (*SI Appendix*, Fig. S1). We measured ^{3}He/^{4}He of >280 distinct samples from these 196 springs (Dataset S1) plus numerous replicates, providing data exceeding our stringent quality criteria (*Materials and Methods*) for 168 spring systems. We supplement our own measurements with previously published data from 29 additional sites, mostly further south (Nepal/India) or north (Tarim/Qaidam).

We measured the ^{3}He/^{4}He ratio (R) of each sample and ratioed it to that in air ($R_A = 1.384 \times 10^{-6}$), giving R/R_A (Fig. 2). We correct for atmospheric contributions using the He/Ne of
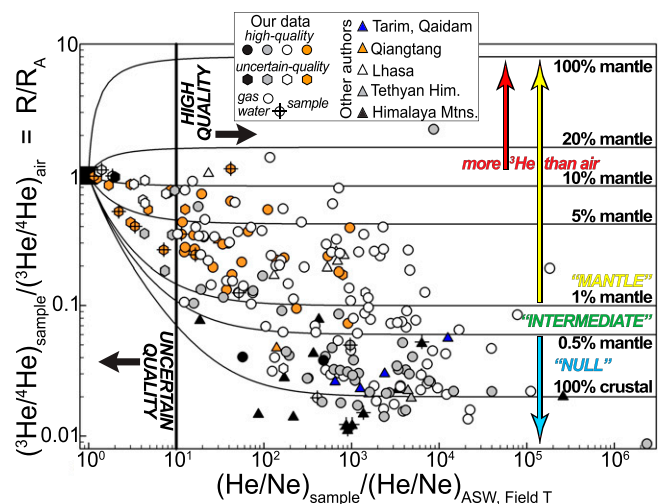
Fig. 2. Isotopic data by Tibetan terrane. R/R_A plotted against $(He/Ne)_{sample}/(He/Ne)_{ASW, Field T}$. Circles: our "high-quality" data separated by a vertical line at $(He/Ne)_{sample}/(He/Ne)_{ASW, Field T} = 10$ from hexagons: our "uncertain-quality" data; triangles: all "high-quality" data from other authors. Locations: blue: Tarim and Qaidam Basins; orange: Qiangtang terrane (includes one Songpan-Ganzi spring); white: Lhasa terrane; gray: Tethyan Himalaya; black: Greater, Lesser, and Sub-Himalaya; crosses indicate water samples. Data are superimposed on mixing curves of three end-member components [mantle = $8R_A$ and $10^5(He/Ne)_{ASW}$, crust = $0.02R_A$, $10^5(He/Ne)_{ASW}$, and ASW = $0.985R_A$ (black square)]. Our "null," "intermediate," and "mantle" designations are separated at 0.5% and 1% mantle contributions (corresponding to $R/R_A = 0.06$ and 0.1 at high He/Ne values); red, yellow, blue, and green arrows and lettering correspond to colors in Fig. 3. *SI Appendix*, Fig. S2 shows these data after air correction (plotting R_C/R_A instead of R/R_A). All plotted data are listed in Dataset S1 but only "high-quality" points are plotted in Fig. 3.

air-saturated water (ASW) at the actual temperature, elevation, and salinity of each spring [hereafter (He/Ne)$_{ASW, Field\ T}$], giving R_C/R_A (9, 18) (Fig. 3 and *SI Appendix*, Fig. S2). The mid-ocean ridge basalt mantle end-member is $8 \pm 1R_A$ (18–21), so samples with $R_C > 0.1R_A$ have >1% of their helium derived from the mantle. Samples with $R_C > 0.1R_A$, despite their continuous dilution by radiogenic ^{4}He during transport or storage (22, 23), indicate the unambiguous, recent addition of mantle volatiles (18–22) and are here called "mantle" samples. We only report samples as "mantle" if $R_C > 0.1R_A$ and if (He/Ne)$_{sample}$/(He/Ne)$_{ASW, Field\ T} > 10$ and if $[O_2] < 1\%$ (Fig. 2 and Dataset S1). R_C values $\leq 0.1R_A$ are considered ambiguous. The ^{3}He/^{4}He production ratio in Earth's crust varies from 0.01 to 0.05R_A (18–22) but is canonically 0.02R_A (18–20), implying that any sample with $R_C > 0.02R_A$ must contain a lithiogenic, tritiogenic, or mantle component. Our null hypothesis is that there should be no mantle helium component at the surface of Earth's thickest crust. In order to essentially preclude false positives (false identification of samples as "mantle") at the expense of accepting some false negatives (failing to recognize actual "mantle" samples), we term samples with $0.06R_A < R_C \leq 0.1R_A$ "intermediate" and samples with $R_C \leq 0.06R_A$ as "null," or of crustal composition. Any cutoff value is arbitrary, but our choice of 0.06R_A and 0.1R_A is supported by the bimodal distribution of sample values (Fig. 3C and *SI Appendix*, Fig. S3) and is consistent with previous helium studies in Tibet and surrounding regions (11, 12, 20, 23). Our helium boundary is robust to different assumptions: Halving or doubling the cutoff values between categories does not materially affect our interpretations (*SI Appendix*, Fig. S3B).

Regional release of primordial ^{3}He from the mantle across large tectonic provinces requires incipient partial melting (11, 12, 19) and/or a flux of metasomatic fluids (21, 24, 25) and may be enhanced by pervasive strain (19, 20, 25) that assists fluid segregation (26). Less than 0.5% of metasomatic water is needed to lower the mantle solidus to 850 °C at 75- to 100-km depth (27). Melt interconnection and melt mobility should prevail down to the coldest temperatures of $(CO_2 + H_2O)$-assisted melting, certainly down to 0.1 vol % melt (28). Even trace melting ($\sim$0.01%) very efficiently extracts ^{3}He from mantle minerals because of its strong incompatibility (partition coefficient $\sim$10^{-4}) (29). Helium also partitions into metasomatic aqueous fluids to which the upper mantle is permeable at $\geq$800 °C if the fluids are even slightly saline (1% NaCl) (30).

Both temperature and age make Indian lithosphere an implausible source for mantle degassing. Indian crust now subducting beneath the Himalaya or underplating beneath Tibet is cold (Fig. 1 *A* and *B*), with Moho temperature of $\sim$420 to 520 °C (13, 31) beneath the Himalayan front. Warming during underthrusting is so slow that the Indian Moho temperature would only reach 650 to 700 °C beneath the Banggong-Nujiang Suture (13), temperatures sufficient for dehydration and decarbonation reactions but still too low to release helium from mantle minerals. Moreover, Indian lithosphere is Paleoproterozoic to Archaean in age (13, 31) so should exhibit highly elevated $[^4$He$]$ and helium isotopic values consistent with canonical crustal production rates (i.e., $\sim$0.02R_A).

In contrast, Tibetan mantle is hot and has a Tertiary tectonothermal age as shown by mantle-sourced potassic and ultrapotassic volcanism spanning the Tibetan Plateau (32). Active volcanism in the northern Qiangtang and Songpan-Ganzi terranes (Fig. 3) suggests Moho temperatures $\geq$1,150 °C (33). Tibetan mantle has also been metasomatized by CO_2 and H_2O first from the subduction of Tethyan oceanic crust then from

India's carbonate-rich passive continental margin and the Indian crustal basement with $\sim$1% water (31), as shown by the isotopic contributions from the Indian lithosphere to Neogene volcanics (32). The hot, metasomatized Tibetan mantle wedge above and north of Indian lithosphere is a viable source of ^{3}He enrichment. Hence, the surface trace of the mantle suture should be marked by a transition between a region of "null" values (i.e., $\leq$0.06R_A) above old, cold (<700 °C) Indian lithosphere (whether crust or mantle) and a region with widespread "mantle" samples (i.e., >0.1R_A) above the hotter (>$\sim$850 °C), H_2O- and CO_2-enriched, incipiently molten Tibetan mantle wedge.

Mapping the Mantle Suture. Fig. 3 includes 86 springs spanning 1,200 km that have unequivocal recent input of primordial ^{3}He from the upper mantle ($\geq$0.1R_A) (*SI Appendix*, Table S1). At the scale of the entire orogen (at least 80° to 92°E) we can draw a sharp boundary line between these "mantle" springs to the north and 90 "null" springs to the south. This preferred boundary includes offsets beneath surface rifts and cleanly separates two distinct populations of samples (Fig. 3C and *SI Appendix*, Fig. S2A), lying as it does south of 99% (all but one) of the "mantle" samples and north of 94% (all but five) of the "null" samples from the Himalaya and Tibet plateau. It also cross-cuts surface geological features including crustal terrane boundaries, thereby implying the bimodality arises in the mantle. Alternative interpretations of the data that we considered included a straight-line transition zone more than one crustal-thickness (>75-km) wide that can achieve an equally good separation of "mantle" from "null" samples only if it encompasses, hence fails to honor, >20% of the individual springs (Fig. 3). Alternate boundaries, for example drawn strictly parallel to the Yarlung-Zangbo Suture (YZS) (11, 12), also honor many fewer high-confidence data points (*SI Appendix*, Fig. S7).

In contrast to the clear spatial organization of R_C/R_A values (Fig. 3) there is little geographical organization that would suggest control by other physicochemical parameters (*SI Appendix*, Fig. S4). We see no spatial control on pH, conductance, $[CO_2]$, or $[CO_2]/[^3$He$]$. The scarcity of high-temperature springs in northern Tibet may suggest the lower topographic relief there does not drive surface fluids to significant depths. A tendency toward higher $[^4$He$]$ content in southern Tibet may correlate with young radiogenic rocks such as the Gangdese batholith and Indian shelf/slope sedimentary rocks and basement in that region. Although high-$[^4$He$]$ fluids require a larger $[^3$He$]$ inventory in order to be recorded as "mantle" samples, the production ratio of $[^3$He$]$ to $[^4$He$]$ in crustal helium ($\sim$0.02 R_A) is independent of [U] and only weakly dependent on [U/Th]. Thus, fluids with high absolute concentration of $[^4$He$]$ also have high $[^3$He$]$, and hence $[^3$He$]/[^4$He$]$ (R/R_A) only varies over two orders of magnitude (Fig. 2) despite $[^3$He$]$ and $[^4$He$]$ each varying by greater than four orders of magnitude (Fig. 3C). The consequent strong correlation of $[^3$He$]$ with $[^4$He$]$ (Fig. 3C) and the minimal correlation of R_C/R_A with $[^4$He$]$ ($r^2 = 0.06$) or spring temperature or other physicochemical spring parameters (*SI Appendix*, Fig. S5) show that neither spring characteristics, nor carrier gases, nor high strain rates, nor proximity to Quaternary volcanic sites (*SI Appendix*, Fig. S5) can explain the geographical organization of ^{3}He/^{4}He values (Fig. 3). We conclude that the plateau-wide helium boundary separates distinct mantle provinces.

This helium boundary places the surface expression of the mantle suture as subparallel to and variably 0 to 170 km north of the YZS from 79 to 91°E and up to 100 km south of the YZS from 91 to 93°E. Given that upward transport of mantle
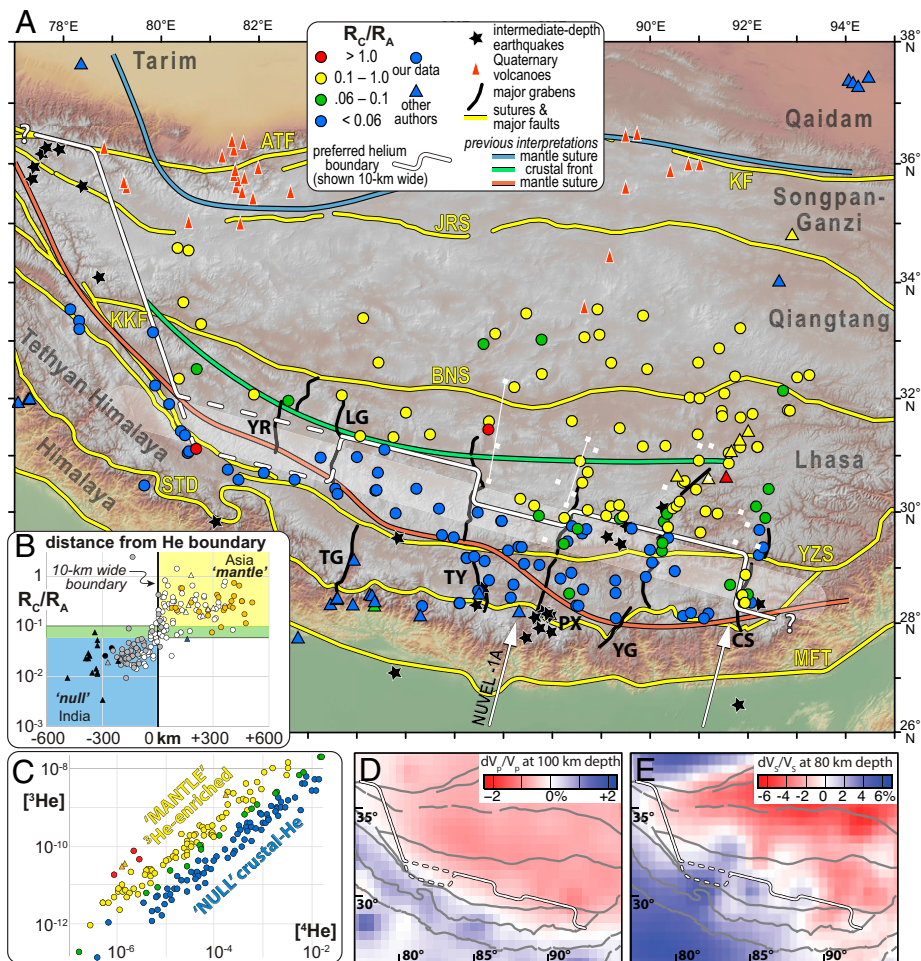
Fig. 3. Distribution of "mantle" and "null" samples. (*A*) ^{3}He/^{4}He isotope data (R_C/R_A); circles and triangles as in Fig. 2, now color-coded red "mantle" samples >1R_A; yellow "mantle" samples >0.1R_A; green "intermediate" samples >0.06R_A; blue "null" samples ≤0.06R_A. Mantle suture: preferred: thin solid white line shows 10-km-wide helium boundary that 1) separates 99% of "mantle" samples from 96% of "null" samples, dashed where data are sparse, 2) separates 65-to-100-km deep earthquakes (black stars) from Quaternary volcanoes (narrow red triangles), and 3) is further constrained to trend 105° orthogonal to plate-convergence vector (white arrows) and be offset only at active rifts (heavy black lines). Alternate interpretation of helium transition shown as 75-km-wide transparent white line. Small white squares: seismic observations of Moho offsets and abrupt upper-mantle velocity transitions (lines linking squares). Yellow lines: sutures/major faults; black lines: normal faults; blue/green/red geophysical boundaries as in Fig. 1*C*. (*B*) R_C/R_A as a function of distance from the preferred 10-km-wide helium boundary (using northern dashed line in *A* and color-coded by terrane affinity as in Figs. 1*C* and 2). All samples in the blue "India" null quadrant, yellow "Asia" mantle quadrant, or green intermediate band fit our preferred model. (*C*) Measured abundance of [^{3}He] vs. [^{4}He] color-coded as in main map, showing clear bimodality (two parallel but clearly separated trend-lines). (*D*) Seismic body-wave tomography, dVp/Vp at 100 km depth (3), same area as *A*, overlain by preferred helium boundary (white line). (*E*) As in *D* but showing adjoint tomography, dVs/Vs at 80 km depth (6). For additional data sources see *SI Appendix,* Fig. S7.

helium through the lithosphere is within a carrier fluid (18, 19) (carbonic, aqueous, or magmatic) by buoyant, hence subverti-cal, ascent (9, 23, 34), this surface expression lies above the actual mantle suture. Fig. 3 also plots all earthquakes with hypocentral depths at 65 to 100 km, thereby including events both close above and below expected Tibetan Moho depth. Brittle-failure earthquakes generally require temperatures at ~70-km depth of ~600 °C (13) and hence mark the presence of cold Indian lithospheric mantle south of the mantle suture (35), though higher strain rates expected near the transition from underplating to subduction may allow earthquakes near the mantle suture to occur at temperatures up to at least 700 °C (36). In contrast, all Quaternary volcanoes in Tibet (Fig. 3)—that suggest higher temperatures, hence the absence of Indian lithosphere, directly below the Tibetan Moho—lie north of our mantle suture. This orogen-scale result requires incipiently melting and/or fluid-fluxed mantle north of the helium boundary and requires that Indian lithosphere does not directly underplate most of Tibet (Fig. 4).

Our preferred helium boundary shown in Fig. 3 (white line) has a location uncertainty ±5 to 75 km (*SI Appendix,* Fig. S3*C*) due to the irregular availability of springs for sampling, but our preferred abrupt boundary segmented at several rifts that paral-lel the plate-convergence direction separates 99% of "mantle" samples from 96% of "null" samples. Our abundant "mantle" samples in Tangra-Yumco (TY), Pumco-Xainza (PX), and Yadong-Gulu (YG) rifts north of the YZS are consistent with the Moho offsets and slab tears or fragmentation previously claimed beneath these rifts from seismological evidence (Fig. 3*A* and *SI Appendix,* Fig. S7). An alternative interpretation to our preferred inference of slab tearing beneath the Cona-Sangri (CS) rift would be that these "mantle" samples reflect ~100-km horizontal transport within the crust along the discontinu-ous normal faults that bound the segmented rift (Fig. 3).

The helium boundary that we associate with the mantle suture is only locally geographically coincident with the Indian crustal front (Fig. 4). The "31°N discontinuity" interpreted as the Indian crustal front (7) (green line, Fig. 3, cf. Fig. 1*B*) is
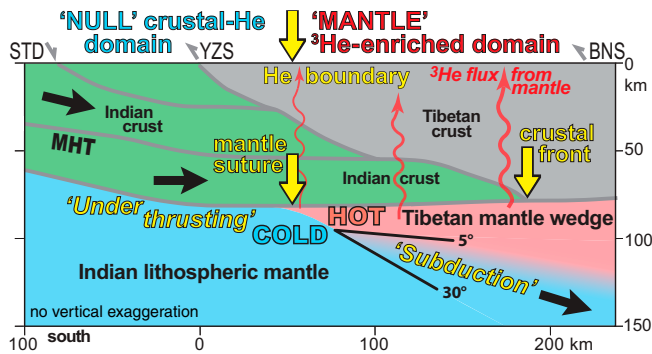
Fig. 4. True-scale cross-section of Tibet at ∼88° to 91°E along yellow swath in Fig. 1*C*. All solid gray lines have been geophysically imaged (23). Mantle suture is interpreted vertically below the boundary between "null" and "mantle" helium domains and its delineation is the main contribution of this paper. Black arrows show relative motion of Indian crust (green) and lithosphere (blue) with respect to fixed Asia (gray). Dip of subducting slab is not constrained by helium studies and likely varies along strike (37, 38), shown here with 5° to 30° dip based on seismic attenuation (1, 39) and tomographic studies (6, 35). Location of the crustal front (northern limit of Indian crust immediately above the Tibetan Moho) varies along strike with respect to the mantle suture, sometimes north of the mantle suture (5) (as shown here), elsewhere coincident with (7), or possibly south of (32, 35), the mantle suture. MHT, Main Himalayan Thrust.

best imaged at 85°E and is there collocated with our helium boundary. Further west seismic data are far less clear but the crustal front has been interpreted (7, 23) further north than our preferred helium boundary at 80°E (Fig. 3). East of 85°E the helium boundary diverges increasingly south of the crustal front (5, 7), by ∼200 to 300 km at 92 to 93°E (Fig. 3), implying delamination of Indian mantle from Indian crust (23) and crustal-scale wedging of Indian crust into Tibetan lithosphere (Fig. 4).

Our preferred interpretation of segmented Indian lithosphere subducting beneath an asthenospheric mantle wedge resolves the spectrum of apparently conflicting seismic data. Regional high ^{3}He/^{4}He observations have been widely linked to low mantle wavespeeds as a proxy for partial melting and/or volatiles (9, 10, 24). We make the same observation across Tibet: Our orogen-scale result is consistent with adjoint-tomographic seismic-wavespeed images (6) and many other body- and surface-wave measurements (3–5, 37, 38) that show lower-wavespeed upper mantle north of our mantle suture than beneath the Himalaya (*SI Appendix*, Fig. S6). Lower-frequency surface-wave tomography may map the northern limit of Indian lithosphere (2, 8) (blue line, Figs. 1*C* and 3), not as previously interpreted directly below Tibetan crust (2, 8), but rather beneath an asthenospheric mantle wedge north of the mantle suture as is suggested by low seismic wavespeeds at ∼100 km depth (35) beneath northern Tibet in this same tomography (2, 8). In contrast, higher-frequency body-wave tomography (3) and combinations of surface- and body-wave methods (37, 38) image the southern limit of incipiently melting or fluid-fluxed mantle at the mantle suture (red line, Figs. 1*C* and 3), and higher-resolution receiver functions image the northern limit of Indian crust (the crustal front) within Tibet (5, 7) (green line, Figs. 1*C* and 3). North of the mantle suture, recent tomographic images (6) show the sub-Tibetan asthenospheric mantle wedge likely extends from 80- to 120-km depth above a ∼10°-dipping slab. Alternatively, shear-wave propagation characteristics (1, 39) suggest the asthenospheric wedge may be much thinner, implying an even shallower-angle subduction so that preexisting Tibetan mantle lithosphere has been displaced and replaced by India, with the exception of a thin

layer of hot therefore weak mantle (Fig. 4). In this view of the India–Asia collision, continental subduction beneath Tibet is conceptually analogous to the modern-day "flat-slab" subduction of the Nazca Ridge for ∼600 km inboard beneath the Peruvian Andes in a region lacking active volcanism, but with the top of the oceanic slab separated from the Andean Moho by a very thin (0 to 20 km) mantle wedge (40).

Discussion

The principal discoveries from our ^{3}He/^{4}He study of 225 geothermal springs across the Tibetan Plateau and Himalaya are that there is widespread mantle degassing through Earth's thickest crust in Tibet, but not through the Himalaya, and that a sharp helium boundary is broadly subparallel to the YZS, ranging from ∼150 km north to ∼100 km south of the suture. We interpret this helium boundary to overlie the "mantle suture" where cold underplated Indian lithospheric mantle is juxtaposed against sub-Tibetan Plateau mantle that is hot and/or fluid-fluxed (asthenospheric mantle wedge). The region in southeastern Tibet where the mantle suture lies 100 km south of the YZS is particularly interesting because the lack of Indian mantle lithosphere between the mantle suture and the surficial suture (YZS) requires delamination of the mantle lithosphere from the Indian crust (5) (Fig. 4). East of Lhasa (90° E) the helium boundary or transition may project southeast as it approaches the Burma subduction zone.

West of the intersection of the YZS and Karakoram fault (80°E) the helium boundary likely turns northwest toward the Hindu Kush salient, west of the active west-Kunlun volcanoes but east of a cluster of deep earthquakes (Fig. 3) including mantle seismicity terminating at the Altyn Tagh fault which marks the mantle suture and northern limit of Indian underthrusting at 78°E (13, 41).

Our improved location of the geochemically identified mantle suture reconciles diverse and conflicting geophysical interpretations and suggests that some of the complex geodynamic models based on along-orogen variability interpreted largely from seismic data (42) warrant reexamination. Similarly one might reconsider whether the gradual change from dominantly extensional faulting in southern Tibet to dominantly strike-slip faulting in central Tibet (*SI Appendix*, Fig. S6E) is controlled by the northern limit of a supposed rigid Indian crust (Indian crustal front) beneath Tibetan crust (14) or by the southern limit of a weak mantle wedge at the mantle suture, or both. We suggest the weak mantle wedge may be more significant in explaining reduced intraplate coupling north of the mantle suture where the subducting plate ceases to exert strong tractions on the overriding plate.

Our ^{3}He/^{4}He data can only constrain the modern location of the mantle suture but in so doing provide a vital benchmark for ongoing controversies about how and when subduction advance or slab rollback have created fundamental shifts in the style of the Himalayan orogen (32, 43). Slab tearing that is a well-attested aspect of oceanic subduction (21, 34, 40) can now be more directly studied in subducting continental crust through precise mapping of the mantle suture and its along-strike offsets (Fig. 3).

Materials and Methods

Field Methods. We have sampled gas (or if not possible, water) from 196 distinct (separated by >1 km) cold, warm, and boiling springs that combine with published data to build a dataset of 225 individual springs across Tibet (Dataset S1). Where multiple outlets were present we typically sampled two of the

strongest gas (bubble) flows within the highest-temperature water of highest conductivity. Gas and water samples were collected in refrigeration-grade copper tubes flushed in-line with >50 volumes of sample fluid prior to sealing with stainless steel clamps (44).

Some geothermal springs are single outlets (*SI Appendix*, Fig. S1 *E, F, G, and I*); others have many tens of spring vents spread continuously over hundreds of meters (*SI Appendix*, Fig. S1 *A–D and H and Table S1*). We report all outlets within 1 km as a single spring unless they lie in different drainages or have clearly distinct field parameters (e.g., temperature, conductance, pH). Samples >1 km apart, even when along a single fault or river valley, are reported separately. Spring temperatures ranged from 6 to 93 °C (*SI Appendix*, Fig. S5A), plus one fumarole, and two well-head samples at 105 °C and 195 °C (#34 ZGR08 and #100 ZDX14). We collected samples at elevations from 1,934 to 5,634 m above sea level (data from other authors extends down to 307 m above sea level in the Subhimalaya) (*SI Appendix*, Fig. S5H). pH ranges from 6.2 to 9.9 (or as low as 6.0 for data from other authors) and conductance from 0.14 to 14 mS (*SI Appendix*, Fig. S5 *B and C*). All high-quality "mantle" samples separated by >25 km are listed in *SI Appendix*, Table S1, and complete data are listed in Dataset S1.

Laboratory Methods. Fluid samples were extracted from the copper tube on a vacuum line and sonicated for ~30 min to ensure complete transfer of dissolved gases from the extraction vessel to the sample inlet line (45). Major gas components (CO_2, N_2, O_2, Ar, CH_4) were measured at Ohio State University using an SRS Residual Gas Analyzer 300 AMU quadrupole mass spectrometer and a Thermo Fisher Trace 1310 gas chromatograph equipped with a thermal conductivity detector and flame ionization detector (44, 46). Average precision values for each analyte, based on repeated measurements of the Lake Erie Air and DCG Partnership and Praxair natural-gas reference materials, are as follows: [N_2] $\pm 1.91\%$, [CO_2] $\pm 2.07\%$, [Ar] $\pm 2.38\%$, and [CH_4] $\pm 2.56\%$. Noble-gas elemental and isotopic compositions were measured and corrected (47) using a Thermo Fisher Helix SFT noble-gas mass spectrometer (44, 48). [^{4}He], [^{22}Ne], and [^{36}Ar] concentrations were determined by comparison to monometrically calibrated aliquots of the internal but cross-referenced (49) Lake Erie Air reference material. Average external precision for noble-gas isotope concentrations based on known–unknown standards were ^{4}He 1.26%, ^{22}Ne 1.93%, and ^{36}Ar 0.96%. Helium isotopic values were determined by comparison to Lake Erie Air and the Scripps Institute of Oceanography MM gas reference materials. Average isotopic errors for helium were approximately ± 0.0096 times the ratio of air for ^{3}He/^{4}He (or 1.330×10^{-8}). Helium and neon isotope ratios were corrected for HD^+, $^{20}NeH^+$, $^{40}Ar^{2+}$, and CO_2^{2+} interferences (47, 50). The average isotopic errors are ^{20}Ne/^{22}Ne $< \pm 0.49\%$, ^{21}Ne/^{22}Ne $< \pm 0.96\%$, ^{38}Ar/^{36}Ar $< \pm 0.89\%$, and ^{40}Ar/^{36}Ar $< \pm 0.56\%$. One hundred seventy-six of the noble-gas data reported from our 196 distinct springs were analyzed at Ohio State University; the remaining 20 samples were analyzed elsewhere (Dataset S1) using substantially similar methods.

Atmospheric Corrections. Atmospheric ^{3}He is accounted for and corrected by measuring the atmospheric abundances of air-saturated noble gases (e.g., ^{20}Ne) in crustal fluids and calculating R_C/R_A, which is the ratio of the measured value of ^{3}He/^{4}He to the equivalent ratio in air (R_A, 1.384×10^{-6}) after correction using the solubility of ^{4}He/^{20}Ne in ASW calculated using the field-measured parameters spring temperature, salinity, and elevation. These R_C/R_A values are on average $0.001R_A$ lower than $(R_C/R_A)_{Static\ T}$ calculated with a static ASW composition assuming 45 °C, salinity = 0.01 per mil and elevation 4,700 m. Similarly, $(He/Ne)_{ASW,\ Field\ T}$ values are on average 0.06 $\log_{10}$ units lower than $(He/Ne)_{ASW,\ Static\ T}$. Our approach is similar to the X-factor (9, 20, 21) but is a more conservative correction, mostly reducing $(He/Ne)_{ASW,\ Static\ T}$ values, and excluding data points with $(He/Ne)_{sample}/(He/Ne)_{ASW,\ Field\ T} \leq 10$ using the geologically more reasonable choice of ASW, rather than air, contamination.

Data Availability. All study data are included in the article and/or supporting information.

Author affiliations: ^{a}Department of Geophysics, Stanford University, Stanford, CA 94305; ^{b}Key Laboratory of Continental Collision and Plateau Uplift, Institute of Tibetan Plateau Research, Chinese Academy of Sciences, Beijing 100101, China; ^{c}School of Earth Sciences, The Ohio State University, Columbus, OH 43210; ^{d}Department of Earth and Planetary Sciences, University of New Mexico, Albuquerque, NM 87131; and ^{e}Scripps Institution of Oceanography, La Jolla, CA 92093

1. M. Barazangi, J. Ni, Velocities and propagation characteristics of Pn and Sn beneath the Himalayan arc and Tibetan plateau: Possible evidence for underthrusting of Indian continental lithosphere beneath Tibet. *Geology* **10**, 179–185 (1982).
2. D. McKenzie, J. Jackson, K. Priestley, Continental collisions and the origin of subcrustal continental earthquakes. *Can. J. Earth Sci.* **56**, 1101–1118 (2019).
3. C. Li, R. D. van der Hilst, A. S. Meltzer, E. R. Engdahl, Subduction of the Indian lithosphere beneath the Tibetan Plateau and Burma. *Earth Planet. Sci. Lett.* **274**, 157–168 (2008).
4. A. Replumaz, F. Funiciello, R. Reitano, C. Faccenna, M. Balon, Asian collisional subduction: A key process driving formation of the Tibetan Plateau. *Geology* **44**, 943–946 (2016).
5. D. Shi et al., Receiver function imaging of crustal suture, steep subduction, and mantle wedge in the eastern India–Tibet continental collision zone. *Earth Planet. Sci. Lett.* **414**, 6–15 (2015).
6. M. Chen et al., Lithospheric foundering and underthrusting imaged beneath Tibet. *Nat. Commun.* **8**, 15659 (2017).
7. J. Nábělek et al., Underplating in the Himalaya-Tibet collision zone revealed by the Hi-CLIMB experiment. *Science* **325**, 1371–1374 (2009).
8. K. Priestley, D. McKenzie, The relationship between shear wave velocity, temperature, attenuation and viscosity in the shallow part of the mantle. *Earth Planet. Sci. Lett.* **381**, 78–91 (2013).
9. L. Hoke, D. R. Hilton, S. H. Lamb, K. Hammerschmidt, H. Friedrichsen, ^{3}He evidence for a wide zone of active mantle melting beneath the Central Andes. *Earth Planet. Sci. Lett.* **128**, 341–355 (1994).
10. Y. Sano, J. Nakajima, Geographical distribution of ^{3}He/^{4}He ratios and seismic tomography in Japan. *Geochem. J.* **42**, 51–60 (2008).
11. L. Hoke, S. Lamb, D. R. Hilton, R. J. Poreda, Southern limit of mantle-derived geothermal helium emissions in Tibet: Implications for lithospheric structure. *Earth Planet. Sci. Lett.* **180**, 297–308 (2000).
12. M. Zhang, Z. Guo, L. Zhang, Y. Sun, Z. Cheng, Geochemical constraints on origin of hydrothermal volatiles from southern Tibet and the Himalayas: Understanding the degassing systems in the India-Asia continental subduction zone. *Chem. Geol.* **469**, 19–33 (2017).
13. T. J. Craig, A. Copley, J. Jackson, Thermal and tectonic consequences of India underthrusting Tibet. *Earth Planet. Sci. Lett.* **353**, 231–239 (2012).
14. A. Copley, J. P. Avouac, B. P. Wernicke, Evidence for mechanical coupling and strong Indian lower crust beneath southern Tibet. *Nature* **472**, 79–81 (2011).
15. W. Tong et al., *Thermal Springs in Tibet* [in Chinese] (Science Press, Beijing, 2000).
16. S. Ge, Q. B. Wu, N. Lu, G. L. Jiang, L. Ball, Groundwater in the Tibet Plateau, western China. *Geophys. Res. Lett.* **35** (L18403), 1–5 (2008).
17. M. P. Hochstein, Z. Yang, "Modelling of terrain-induced advective flow in Tibet: Implications for assessment of crustal heat flow" in *Proceedings of the Seventeenth Workshop on Geothermal Reservoir Engineering* (Stanford University, Stanford, CA, 1992), pp. 153–157.
18. C. J. Ballentine, R. Burgess, B. Marty, Tracing fluid origin, transport and interaction in the crust. *Rev. Mineral. Geochem.* **47**, 539–614 (2002).
19. D. R. Hilton, Geochemistry. The leaking mantle. *Science* **318**, 1389–1390 (2007).
20. M. Zhang et al., Linking deeply-sourced volatile emissions to plateau growth dynamics in southeastern Tibetan Plateau. *Nat. Commun.* **12**, 4157 (2021).
21. C. D. Hiett, D. L. Newell, M. J. Jessup, ^{3}He evidence for fluid transfer and continental hydration above a flat slab. *Earth Planet. Sci. Lett.* **556**, 116722 (2021).
22. T. Torgersen, S. Drenkard, M. Stute, P. Schlosser, A. Shapiro, Mantle helium in ground waters of eastern North America: Time and space constraints on sources. *Geology* **23**, 675–678 (1995).
23. S. L. Klemperer et al., Mantle fluids in the Karakoram fault: Helium isotope evidence. *Earth Planet. Sci. Lett.* **366**, 59–70 (2013).
24. L. J. Crossey et al., Continental smokers couple mantle degassing and unique microbiology within continents. *Earth Planet. Sci. Lett.* **435**, 22–30 (2016).
25. B. M. Kennedy, M. C. van Soest, Flow of mantle fluids through the ductile lower crust: Helium isotope trends. *Science* **318**, 1433–1436 (2007).
26. D. L. Kohlstedt, B. K. Holtzman, Shearing melt out of the Earth: An experimentalist's perspective on the influence of deformation on melt extraction. *Annu. Rev. Earth Planet. Sci.* **37**, 561–593 (2000).
27. R. Dasgupta, Volatile-bearing partial melts beneath oceans and continents–Where, how much, and of what compositions? *Am. J. Sci.* **318**, 141–165 (2018).
28. E. Gardès, M. Laumonier, M. Massuyeau, F. Gaillard, Unravelling partial melt distribution in the oceanic low velocity zone. *Earth Planet. Sci. Lett.* **540**, 116242 (2020).
29. C. R. Jackson, S. W. Parman, S. P. Kelley, R. F. Cooper, Constraints on light noble gas partitioning at the conditions of spinel-peridotite melting. *Earth Planet. Sci. Lett.* **384**, 178–187 (2013).
30. Y. Huang, T. Nakatani, M. Nakamura, C. McCammon, Experimental constraint on grain-scale fluid connectivity in subduction zones. *Earth Planet. Sci. Lett.* **552**, 116610 (2020).

31. P. Henry, X. Le Pichon, B. Goffé, Kinematic, thermal and petrological model of the Himalayas: Constraints related to metamorphism within the underthrust Indian crust and topographic elevation. *Tectonophys.* **273**, 31–56 (1997).

32. Z. Guo, M. Wilson, Late Oligocene–early Miocene transformation of postcollisional magmatism in Tibet. *Geology* **47**, 776–780 (2019).

33. Q. Wang *et al.*, Pliocene-Quaternary crustal melting in central and northern Tibet and insights into crustal flow. *Nat. Commun.* **7**, 11888 (2016).

34. D. R. Hilton, H. Craig, A helium isotope transect along the Indonesian archipelago. *Nature* **342**, 906–908 (1989).

35. K. Priestley, J. Jackson, D. McKenzie, Lithospheric structure and deep earthquakes beneath India, the Himalaya and southern Tibet. *Geophys. J. Int.* **172**, 345–362 (2008).

36. P. Molnar, The brittle-plastic transition, earthquakes, temperatures, and strain rates. *J. Geophys. Res.* **125**, e2019JB019335 (2020).

37. M. R. Agius, S. Lebedev, Tibetan and Indian lithospheres in the upper mantle beneath Tibet: Evidence from broadband surface-wave dispersion. *Geochem. Geophys. Geosyst.* **14**, 4260–4281 (2013).

38. C. Nunn, S. W. Roecker, K. F. Priestley, X. Liang, A. Gilligan, Joint inversion of surface waves and teleseismic body waves across the Tibetan collision zone: The fate of subducted Indian lithosphere. *Geophys. J. Int.* **198**, 1526–1542 (2014).

39. J. Barron, K. Priestley, Observations of frequency-dependent Sn propagation in Northern Tibet. *Geophys. J. Int.* **179**, 475–488 (2009).

40. S. K. Antonijevic *et al.*, The role of ridges in the formation and longevity of flat slabs. *Nature* **524**, 212–215 (2015).

41. S. Wang, S. L. Klemperer, Love-wave normal modes discriminate between upper-mantle and crustal earthquakes: Simulation and demonstration in Tibet. *Earth Planet. Sci. Lett.* **571**, 117089 (2021).

42. P. Huangfu *et al.*, Multi-terrane structure controls the contrasting lithospheric evolution beneath the western and central-eastern Tibetan plateau. *Nat. Commun.* **9**, 3780 (2018).

43. P. Kapp, P. G. DeCelles, Mesozoic–Cenozoic geological evolution of the Himalayan-Tibetan orogen and working tectonic hypotheses. *Am. J. Sci.* **319**, 159–254 (2019).

44. W. K. Eymold *et al.*, Hydrocarbon-rich groundwater above shale-gas formations: A Karoo basin case study. *Ground Water* **56**, 204–224 (2018).

45. T. H. Darrah, A. Vengosh, R. B. Jackson, N. R. Warner, R. J. Poreda, Noble gases identify the mechanisms of fugitive gas contamination in drinking-water wells overlying the Marcellus and Barnett Shales. *Proc. Natl. Acad. Sci. U.S.A.* **111**, 14076–14081 (2014).

46. M. T. Moore *et al.*, Differentiating between biogenic and thermogenic sources of natural gas in coalbed methane reservoirs from the Illinois Basin using noble gas and hydrocarbon geochemistry. *Geol. Soc. Lond. Spec. Publ.* **468**, 151–188 (2018).

47. T. H. Darrah, R. J. Poreda, Evaluating the accretion of meteoritic debris and interplanetary dust particles in the GPC-3 sediment core using noble gas and mineralogical tracers. *Geochim. Cosmochim. Acta* **84**, 329–352 (2012).

48. R. L. Kreuzer *et al.*, Structural and hydrogeological controls on hydrocarbon and brine migration into drinking water aquifers in southern New York. *Ground Water* **56**, 225–244 (2018).

49. M. Kang *et al.*, Identification and characterization of high methane-emitting abandoned oil and gas wells. *Proc. Natl. Acad. Sci. U.S.A.* **113**, 13636–13641 (2016).

50. D. Gyore, A. Tait, D. Hamilton, F. M. Stuart, The formation of NeH$^+$ in static vacuum mass spectrometers and re-determination of ^{21}Ne/^{20}Ne of air. *Geochim. Cosmochim. Acta* **263**, 1–12 (2019).